Check for updates

Water Science & Technology

IWA PUBLISHING

© 2022 The Authors

Water Science & Technology Vol 85 No 5, 1384 doi: 10.2166/wst.2022.047

Novel design of amine and metal hydroxide functional group modified onto sludge biochar for arsenic removal

Chih-Kuei Chen[a,b], Nhat-Thien Nguyen[c], Thuy-Trang Le[d], Cong-Chinh Duong[e], Cong-Nguyen Nguyen[f], Duc-Toan Truong[g] and Chun-Hsing Liao[h,*]

[a] Department of Environmental Engineering, National I-Lan University, Ilan 26047, Taiwan, China
[b] Continental Water Engineering Corporation, Taipei 10608, Taiwan, China
[c] Department of Chemical Engineering and Biotechnology, National Taipei University of Technology, Taipei 10608, Taiwan, China
[d] Faculty of Environment and Chemical Engineering, Duy Tan University, Da Nang 500000, Viet Nam
[e] Southern Institute of Water Resources Research, Ho Chi Minh 700000, Viet Nam
[f] Faculty of Chemistry and Environment, Dalat University, Dalat 66100, Viet Nam
[g] Dalat Nuclear Research Institute, Dalat 66100, Viet Nam
[h] Infectious Disease Divisions, Far Eastern Memorial Hospital, New Tai-Pei 22060, Taiwan, China
*Corresponding author. E-mail: liaochunhsing@gmail.com

C-CD, 0000-0001-7862-6802

ABSTRACT

This study involved novel-designed sludge biochar (SB) adsorbed for arsenic removal with lower operating costs and higher adsorption efficiency properties. Generally, biochar only relies on micropores for pollutant adsorption, but physical adsorption is not highly efficient for arsenic removal. Therefore, in order to improve the removal efficiency of arsenic by SB, diethylenetriamine (DETA) and $FeCl_3$ were used in this study to modify the surface of SB by an immersion method. The objectives of this research are to obtain optimum operation conditions by assessing the effect of different Fe content, pH and initial concentration on adsorbing arsenic. This study is the first to use Density Functional Theory (DFT) to simulate and verify the adsorption mechanism of arsenic by SB. Results showed the presence of amine/iron oxyhydroxides functional groups greatly promoted SB surface activity and its arsenic adsorption potential. The surface area, pore volume and pore size of the SB were estimated to be 525 $m^2 g^{-1}$, 0.35 $cm^3 g^{-1}$ and 8.71 nm, respectively. The DFT model result is the same as the result of arsenic adsorption performance with high adsorption energy (−246.3 $kJmol^{-1}$) and shorter bond distances (1.42 Å), indicating strong chemical adsorption between arsenic and material. The reaction mechanism is divided into four pathways, including oxidation-reduction, complexation, electrostatic adsorption and pore adsorption.

Key words: arsenic, density functional theory, Fe-SB-DETA, sludge biochar

HIGHLIGHTS

- Novel design of amine-metal hydroxide group composite material.
- Composite material has lower costs and higher adsorption efficiency.
- This study is the first to use Density Functional Theory (DFT) to simulate and verify the adsorption mechanism of arsenic by sludge biochar.
- The adsorption mechanism of iron oxyhydroxides functional groups and arsenic was used density functional theory.
- Composite material has four adsorption pathways.

INTRODUCTION

Warming of the earth is considered as the major adverse effect of climate change along with other abnormalities such as non-availability of water resources, rise in seawater level, glaciers melting, and loss of biodiversity. Over the years, decreased agriculture production and water quality degradation have been observed due to climatic abnormalities. Crop production is highly sensitive to climate. It is affected by long-term trends in average rainfall and temperature, annual climate variations, shocks during different stages of growth, and extreme weather events (Srivastav *et al.* 2021). Therefore, water recycling and water conservation is one of the sustainable development goals. Heavy metals are one of the most hazardous inorganic contaminants of both water and soil environment composition. Normally, heavy metals are non-biodegradable in nature because

This is an Open Access article distributed under the terms of the Creative Commons Attribution Licence (CC BY 4.0), which permits copying, adaptation and redistribution, provided the original work is properly cited (http://creativecommons.org/licenses/by/4.0/).

Downloaded from http://iwaponline.com/wst/article-pdf/85/5/1384/1021040/wst085051384.pdf
by guest

of their long persistence in the environment. Trace amounts of heavy metal contamination may pose severe health problems in human beings after prolonged consumption (Kanwar *et al.* 2020).

Arsenic is a concern in groundwater or wastewater treatment because of its health effects. Arsenic was classified as a substance that causes serious eye damage (Level 1), cancerogen (Level 1), skin irritating substance (Level 2), reproductive toxic substances (Level 2) and hazardous substances in the water environment (Level 2). Arsenic is primarily used in solutions such as As(V) ($H_2AsO_4^-$, $HAsO_4^{2-}$ and AsO_4^{3-}) and As(III) ($H_2AsO_3^-$, $HAsO_3^{2-}$ and AsO_3^{3-}) (Yang *et al.* 2015). In general, As(III) is more toxic than As(V) because the former binds to single but more closely related groups of nearby sulfhydryls that react with a variety of proteins and inhibit their activity. Owing to electronic configuration As(III) is more stable than As(V) (Aposhian *et al.* 1989; Sahu & Patel 2013). The presence of arsenic in water is attributed to natural weathering processes, geochemical reactions, biological activity, combustion of fossil fuels, volcanic eruptions, gold mining, leaching of man-made arsenic compounds, metal ores smelting, desiccants, wood preservatives and agricultural pesticides, and many other anthropogenic activities (Sahu & Patel 2013). Arsenic is toxic and induces hyper-pigmentation, muscle weakness, skin thickening, neurological disorders and human cancer. The main route of human exposure is drinking arsenic contaminated groundwater. Hence, the arsenic level for drinking water has been reduced by the World Health Organization to 10 $\mu g\ L^{-1}$ (Choong *et al.* 2007).

The approaches for arsenic removal from water sources include chemical precipitation, membrane processes, reverse osmosis, oxidation, ion exchange (Mondal *et al.* 2006, 2013) and electro coagulation treatment (Song *et al.* 2017). Recent research focused on the use of possible adsorbents, many adsorbents were used for arsenic adsorption based on agriculture and industrial waste, surfactants, carbon-based materials, polymers and metal oxides (Kurniawan *et al.* 2012; Ray & Shipley 2015). Especially, metal oxides such as iron-doped amino-functionalized sawdust (Hao *et al.* 2016), isolated ferric ion combined on chelate resin (Aacharya *et al.* 2017), magnetic gelatin modified biochar (Zhou *et al.* 2017), iron hydroxide/manganese dioxide (Xiong *et al.* 2017), activated carbon–alumina composites (Karmacharya *et al.* 2016), zeolite synthesized from cenospheres (Markandeya *et al.* 2021), zero-valent iron nanoparticles (Dong *et al.* 2012; Bhowmick *et al.* 2014), silver nanoparticles (Bhardwaj *et al.* 2021), TiO_2 (Xu *et al.* 2010), CeO_2 (Feng *et al.* 2012), CuO (Reddy *et al.* 2013), Fe_2O_3 (Tang *et al.* 2011a, 2011b), Fe_3O_4 (Akin *et al.* 2012), CaO (Olyaie *et al.* 2012), ZrO_2 (Cui *et al.* 2013), GNPs/$CuFe_2O_4$ (La *et al.* 2017), metal-organic frameworks (Rani *et al.* 2020) and have been extensively studied in aqueous solution for arsenic treatment due to their high affinity with arsenic species, low cost and adsorption capability tunability.

An alternative carbon source is readily available in the form of urban sludge, which is currently managed as a waste in Taiwan. The quantity of waste sludge has been steadily increasing in the country, thus requiring the government to spend a large amount of money for the management of this waste. Therefore, it is important to develop a one step facile and quick preparing method for high efficiency for arsenic removal. Sludge Biochar (SB) has been identified as an effective adsorbent that can be used to remove various heavy metals dissolved in water, because the specific surface area and micro-porous structures of SB are high, while SB hosts several surface functional groups, such as carboxyl (-COOH) and hydroxyl (-OH), for adsorbing heavy metal effectively. These groups can work through electron donation, cation exchange, electrostatic attraction, or surface complexation to effectively remove arsenic. On the other hand, to understand the effect of amine and iron oxyhydroxides functional groups on the SB's surface to adsorb arsenic, diethylenetriamine (DETA) and iron metals were used to modify the SB and improve the effects of arsenic adsorption. In this particular adsorption, the particles of iron oxyhydroxides found on the SB surface are capable of replacing the As molecules OH- ligand, forming mono or bi-dentate complexes that enable them to be attached to the surface. This coordination occurs only in charged molecules previously attracted to the metal-SB surface, or in those molecules with sufficient energy to overcome the electrostatic repulsion with the metal-biochar surface. Thus, electrostatic repulsion between negative surface charge of metal-SB surface and As anions occurs. If these ionic molecules have difficulties in overcoming these electrostatic forces they cannot interact to a higher extent with metal particles and hence adsorption occurs to a lesser extent. Moreover, acidic properties bind efficiently to As molecules allowing electrostatic interactions with metal oxyhydroxide particles and with acidic surface groups (Arcibar-Orozco *et al.* 2014).

Additionally, the mechanism for the adsorption of arsenic on the SB surface is not yet clear. According to the previous study, a theoretical analysis of the mechanism of arsenic adsorption on the surface of SB prepared from urban sludge is hardly available. Therefore, the adsorption mechanism and the impact mechanism of metal oxides complexes on arsenic adsorption over the SB surface of urban sludge are very important (Gao *et al.* 2018). The Density Functional Theory (DFT) has proven to be a successful research tool for adsorption and reaction theoretical analysis. The mechanism for

Downloaded from http://iwaponline.com/wst/article-pdf/85/5/1384/1021040/wst085051384.pdf
by guest

adsorption of arsenic on SB and composites of metal oxides is systematically investigated by DFT calculation in this research. The objectives of this work are: (a) to prepare SB and iron oxides composites, such as SB and Fe-SB-DETA for developing key reaction between arsenic and modified material; (b) to obtain optimum operation conditions by assessing the effect of different Fe content loading mass on adsorbing arsenic; (c) to obtain optimum operation conditions by assessing the effect of pH and initial concentration on adsorbing arsenic; (d) to systematically calculate adsorption energy, bond distance and adsorbed structure through DFT; (e) to developing arsenic adsorption mechanisms.

MATERIALS AND METHODS

Preparation of SB

To obtain the activated SB, this study used $ZnCl_2$ as the activator because $ZnCl_2$ requires a low activation temperature and the best pore-forming effect. First, different amounts of x% $ZnCl_2$ (x = 33, 50, 60 and 67%) were dissolved in 150 mL of distilled water. Then, 10 g of urban sludge was mixed with the $ZnCl_2$ solution and stirred at approximately 85 ± 5 °C for 2 hr. The mixtures were dehydrated in an oven at 110 ± 5 °C for about 24 hr. The $ZnCl_2$ impregnated urban sludge was placed in a quartz tube (diameter: 2.0 cm, length: 70 cm) and pyrolyzed in a horizontal tubular furnace (power: 1000 W) under nitrogen flow. Nitrogen was used to provide an inert atmosphere under flow rate of 60 mL min^{-1}. The samples were heated to final temperatures of 450 ± 5 °C with a heating rate of 10 °C min^{-1} for a residence time of 1 hr in a horizontal tubular furnace. The resultant SB was washed with 3 M HCl solution by heating at around 90 ± 5 °C for 30 min to remove residual $ZnCl_2$. In addition, it was filtered and rinsed by warm distilled water until it reached neutral pH, than dried at 100 ± 5 °C in an oven for about 12 hr and weighed to calculate the yield.

Preparation of Fe-SB-DETA

Fe-SB-DETA was prepared following the method described by Lin *et al.* (2019) and Chen *et al.* (2021). In brief, most of the sludge moisture was removed in the decanter after pretreatment in a calciner for 2 hr to obtain absolute preparation materials. To obtain the activated material, the appropriate amount of 3.3% DETA and different amounts of $FeCl_3$ (including 2.0, 4.0, 8.0, 16.0 and 32.0%) were dissolved in 150 mL of distilled water. Then, 10 g of the SB was mixed with mixture solution, and stirred at 85 ± 5 °C for 2 hr. Then, the mixtures were dehydrated in an oven at 110 ± 5 °C for 24 hr after filtered and rinsed by distilled water. Different composite materials are abbreviated as 2%Fe-SB-DETA, 4%Fe-SB-DETA, 8%Fe-SB-DETA, 16%Fe-SB-DETA and 32%Fe-SB-DETA.

Materials characterization

The specific surface area, pore size distribution and pore volume were determined by performing nitrogen adsorption-desorption measurements with an ASAP 2020 apparatus by using Brunauer-Emmett-Teller (BET) calculation methods. The Fourier Transform Infrared (FTIR, Model: NiCoLET- iS10) of the biochar was recorded to study the functional groups at room temperature. The crystal phase of the biochar was determined by an X-ray Diffraction (XRD, Model: X-Pert PRO) with employing Cu Kα radiation wavelength of 0.15405 nm, accelerating voltage of 40 kV and current of 30 mA over the 2θ range of 20–80°. The interaction oxidation and reduction mechanism of metal ions on biochar was used Electrochemical Techniques (ECT, Model: PGSTAT302N). The metal valence on the surface of biochar was further determined by X-ray photoelectron spectroscopy (XPS, Model: ESCALAB Xi^+).

Adsorption performance assessment

Adsorption isotherm experiments were carried out in a 100 mL batch adsorption system. Arsenic solutions were prepared by adding As_2O_3 (As(III)) from the High-Purity Standards company. The sludge biochar was mixed with 50 mL of the appropriate As(III) solution at 25 °C for 60 min. The solution was filtered using a membrane filter (pore size 0.45 μm). In addition, an inductively coupled plasma atomic emission spectroscopy with a detection limit for arsenic of 10 ppb was used to evaluate the residual arsenic in the aqueous solutions. The test data were regularly calibrated using standard solution in order to obtain accurate data.

The exact amount of adsorbed arsenic per adsorbent unit mass was determined by weight balance as follows Equation (1):

$$q_e = \frac{C_o - C_e}{W} \times V \quad (1)$$

Downloaded from http://iwaponline.com/wst/article-pdf/85/5/1384/1021040/wst085051384.pdf
by guest

where the equilibrium adsorption capacity is q_e (mg g^{-1}), V (mL) is the volume of As solution, W (mg) is the amount of adsorbent used in the experiments, C_o (mg L^{-1}) is the initial concentration of As and the balance concentration measured after adsorption stands for C_e (mg L^{-1}).

Adsorption kinetics

A first order reaction depends on the concentration of only one reactant (a unimolecular reaction). The pseudo-first-order equation is given as follows:

$$\frac{dq_t}{dt} = k_1(q_e - q_t) \tag{2}$$

where q_t is the amount adsorbed at time t (mg g^{-1}), and q_e is the adsorption capacity at equilibrium (mg g^{-1}). In addition, k_1 is the pseudo-first-order rate coefficient (min^{-1}) and t is the contact time (min). The integration of Equation (2) with the initial condition, $q_t = 0$ at $t = 0$, leads to the following Equation (3) (Mahmood *et al.* 2018):

$$\log(q_e - q_t) = \log q_e - \frac{k_1}{2.303}t \tag{3}$$

A second order reaction depends on the concentrations of one second order reactant, or two first order reactants. The pseudo-second-order model is represented as follows:

$$\frac{dq_t}{dt} = k_2\,(q_e - q_t)^2 \tag{4}$$

where k_2 is the pseudo-second-order rate coefficient (mg g^{-1} min^{-1}). Integrating Equation (4) and $q_t = 0$ at $t = 0$, the following Equation (5) is obtained (Mahmood *et al.* 2018):

$$\frac{t}{q_t} = \frac{1}{k_2 q_e^2} + \frac{1}{q_e}t \tag{5}$$

DFT model and computation detail

The SB surface is doped with amine functional group and iron hydroxide group to form other Fe-SB-DETA structures. The arsenic is adsorbed on the above Fe-SB-DETA structures respectively after 10 ns molecular dynamics simulation. Finally, adsorption systems were constructed in the same cubic simulation lattice built with their dimensions of x = 10 Å, y = 10 Å, and z = 14 Å.

In Materials Studio 2018, all the DFT calculations in this analysis were carried out using the DMol^3 software kit (Materials Studio DMoL3 2018). The terms of exchange and correlation were determined in the form proposed by Perdew, Burke, and Ernzerhof using the Generalized Gradient Approximation (Perdew *et al.* 1996). The core DFT semi-core pseudo potential method was utilized to calculate the core treatment of DETA, for other elements the all-electron method was applied (Delley 2002). Solvation effects were incorporated by conductor-like polarizable continuum model for all the systems with water as solvent. The adsorption energy (E_{ads}) of pollutant molecules on Fe-SB-DETA surface was calculated by the following Equation (6) (Hu *et al.* 2017):

$$E_{ads} = E_{Fe-SB-DETA-pollutant} - (E_{Fe-SB-DETA} + E_{pollutant}) \tag{6}$$

where $E_{Fe\text{-}SB\text{-}DETA}$ and $E_{pollutant}$ respectively represent the energies of the Fe-SBC-DETA surface and the single pollutant molecule, and the $E_{Fe\text{-}SB\text{-}DETA\text{-}pollutant}$ is the total energy of pollutant-Fe-SB-DETA complex. According to Equation (2), a negative value of E_{ads} indicates that the process is an exothermic reaction and high negative value corresponds to a stronger interaction, which indicates more heat release and a more stable product. There exist two types of adsorption, if the value of E_{ads} is between −30 and −10 kJ mol^{-1}, the reaction is classified as physical absorption. Otherwise, if the value is between

Downloaded from http://iwaponline.com/wst/article-pdf/85/5/1384/1021040/wst085051384.pdf
by guest

−960 and −50 kJ mol^{-1}, then it belongs to chemical adsorption. Basically, a higher value of E_{ads} corresponds to a stronger adsorption (Gao *et al.* 2018).

RESULTS AND DISCUSSION

Characterization of materials

An N_2 adsorption/desorption isotherm analyzer at liquid nitrogen temperature (77 K) was used to determine the surface area, pore volume, and pore size of SB. The optimal activation ratio of carbonized sludge over $ZnCl_2$ was found to be 1:1. The surface area, pore volume and pore size of the SB-50%$ZnCl_2$ were estimated to be 525 m^2 g^{-1}, 0.35 cm^3 g^{-1} and 8.71 nm, respectively. Fewer activators can not completely manufacture pores of SB, but too much activator fails to create more pores and causes the pores to be blocked and remain on the surface of the material, resulting in a decrease in pore volume and specific surface area. The isotherms belonged to Type IV in the definition of International Union of Pure and Applied Chemistry and indicated that N_2 is condensed in the pores at high relative pressures. There was a hysteresis loop of the H2 style since the pores had a narrow inlet and wide hole, as shown in Figure 1. The surface area and pore volume in this study were higher than the results of Rahman *et al.* (2020) (375.32 m^2 g^{-1} and 0.239 cm^3 g^{-1}) and Mahmood *et al.* (2018) (167 m^2 g^{-1} and 0.16 cm^3 g^{-1}).

The functional groups are very important characteristics of the SB, because they determine the surface properties of the SB and their quality. It can provide basic spectra of SB, especially for the determination of types and intensities of their surface functional groups. The changes in the functional groups of different Fe content and appropriate amount of DETA modified on SB were analyzed by FTIR spectroscopy, as shown in Figure 2. The peak at 3400 cm^{-1} of 8%Fe-SB-DETA is significantly stronger than the peak of other materials. The -OH and N-H stretching vibration band are characteristic peaks of the amine group at about 3400 cm^{-1} (Ma *et al.* 2014). The appearance of peaks at 2849 and 2930 cm^{-1} in the spectrum were attributed to C-H stretching vibration in -CH and -CH_2 (Ma *et al.* 2014). The band at 1620 cm^{-1} can be ascribed to C = C aromatic ring stretching vibration (Kilic *et al.* 2011). The band at 1430–1470 cm^{-1} is ascribed to C-H bending vibrations in CH_3 groups (Ma *et al.* 2014). C = O vibrations at 1000–1100 cm^{-1} are produced by the stretching vibration of the oxygen-containing functional group C = O bond (Jindo *et al.* 2014). There is a weak vibration band between 530 and 765 cm^{-1}, which is judged as an aromatic structure. Due to the large amount of organic matter in the sludge, the chemical structure is composed of a large number of different atoms.

The aim of the XRD studies is to determine the species of SB, SB-DETA and 8%Fe-SB-DETA compounds deposited onto the biochar surface, as shown in Figure 3. The XRD pattern of biochar exhibited one broad diffraction peak corresponding to the diffraction of carbon. A peak at $2\theta = 25°$ was observed for the SB, which was attributed to the carbon in SB (Figure 3(a)). Figure 3(b) shows that the carbon peaks change significantly after using DETA to modify the surface of SB. This is because the carbon peaks become stronger when the carbon in DETA is combined with SB. Compared with that of SB, SB-DETA and 8% Fe-SB-DETA, Fe-O typical peak was observed for 8%Fe-SB-DETA at $2\theta = 36°$ and 57°, respectively, shown in Figure 3(c).

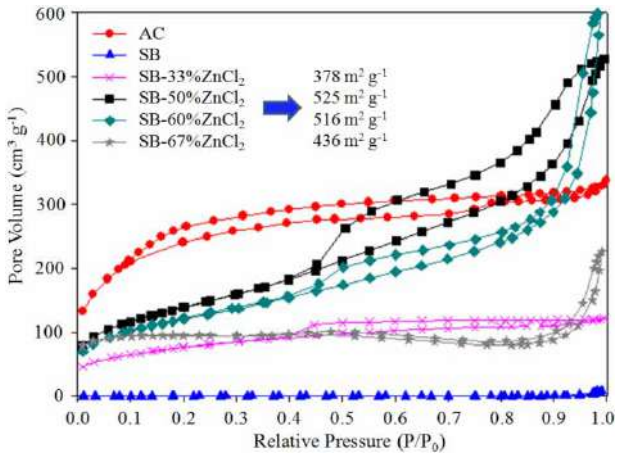

Figure 1 | The N_2 adsorption–desorption isotherm of materials.

Downloaded from http://iwaponline.com/wst/article-pdf/85/5/1384/1021040/wst085051384.pdf
by guest

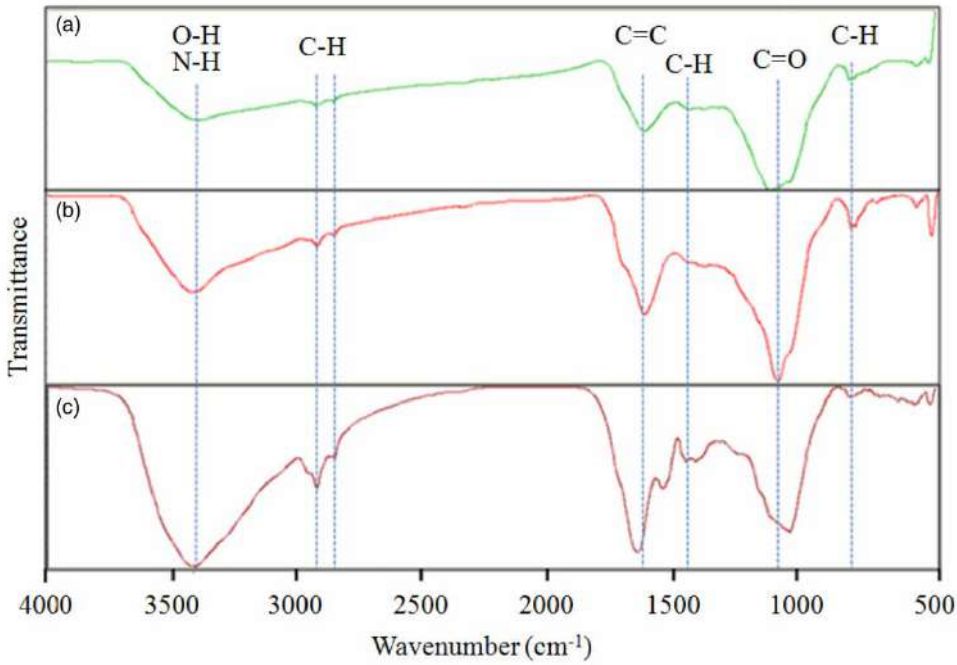

Figure 2 | FTIR spectrums of (a) SB, (b) SB-DETA and (c) 8%Fe-SB- DETA.

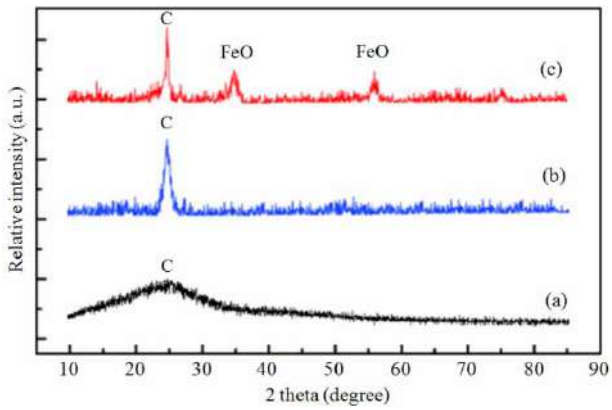

Figure 3 | XRD patterns of (a) SB, (b) SB-DETA and (c) 8%Fe-SB- DETA.

During the present studies, our aim was to look into the difference in the interaction oxidation/reduction mechanism of metal ions on SB using the ECT method. Cyclic Voltammetry (CV) is used to investigate the effect of surface modification, which could provide useful information about the surface states of SB due to the presence of metal vacancy defects on the surface. Figure 4 shows the CV of 2%Fe-SB-DETA, 4%Fe-SB-DETA, 8%Fe-SB-DETA, 16%Fe-SB-DETA and 32%Fe-SB-DETA electrodes in 6 M KOH solution. The bounded area of the CV curve indicates the real active surface area of the anode and the cathode. 8%Fe-SB-DETA (0.00062 mA) shows a higher current than the 16%Fe-SB-DETA (0.00047 mA), 32%Fe-SB-DETA (0.00044 mA), 4%Fe-SB-DETA (0.00031 mA) and 2%Fe-SB-DETA (0.00023 mA) at the anode. Additionally, 8%Fe-SB-DETA (−0.0016 mA) shows a higher current than the 16%Fe-SB-DETA (−0.0012 mA), 32%Fe-SB-DETA (−0.0011 mA), 4%Fe-SB-DETA (−0.0007 mA) and 2%Fe-SB-DETA (−0.0005 mA) at the cathode. This is indicating that 8%Fe-SB-DETA has a larger active point and better oxidation reduction reaction.

Figure 5 shows the linear sweep voltammetry curves of the samples deposited at different potentials. The currents of the 8% Fe-SB-DETA (0.0027 mA) are improved after being compared with that of 2%Fe-SB-DETA (0.00007 mA) and 4%Fe-SB-DETA (0.0006 mA), indicating that the hydrogen evolution over potential with 8%Fe-SB-DETA is lower than that with 2%

Downloaded from http://iwaponline.com/wst/article-pdf/85/5/1384/1021040/wst085051384.pdf
by guest

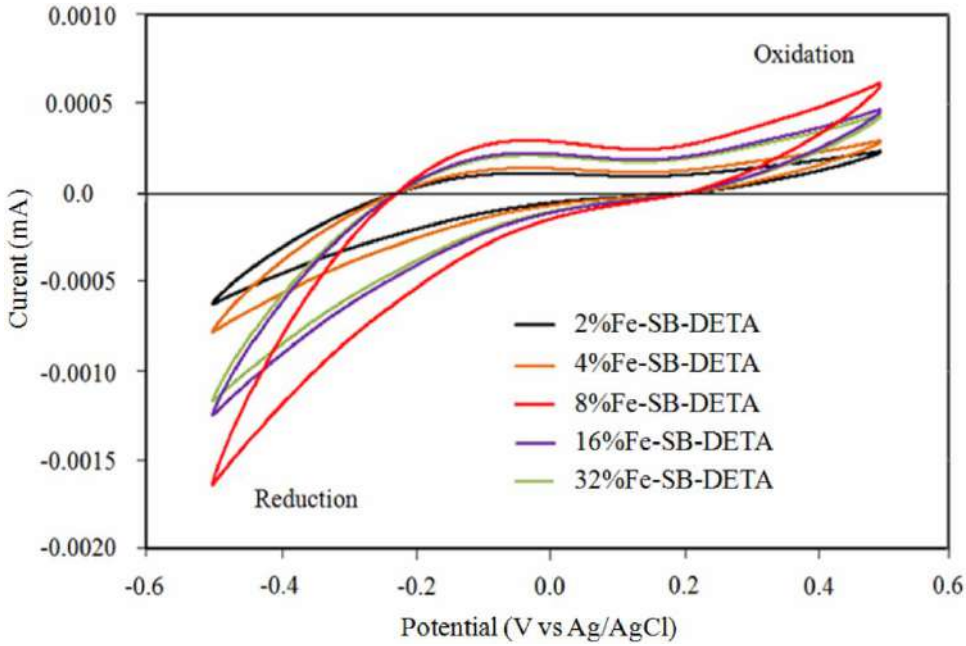

Figure 4 | Cyclic voltammograms of biochar electrodes.

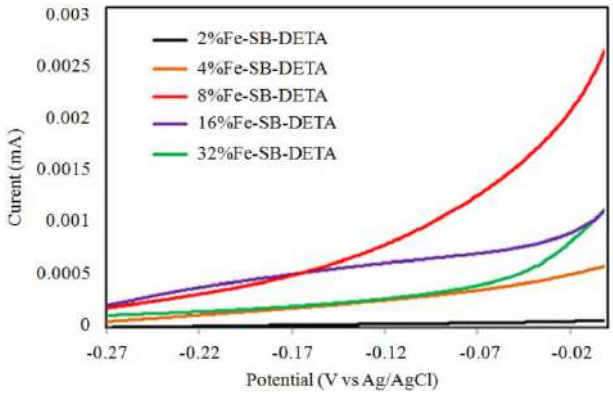

Figure 5 | Linear sweep voltammetry curves at different potentials.

Fe-SB-DETA. As a result, 8%Fe-SB-DETA (0.0027 mA) has larger currents than 16%Fe-SB-DETA (0.0012 mA) and 32%Fe-SB-DETA (0.0011 mA). In addition, 8%Fe-SB-DETA composite interface displays a significant change in current–voltage properties as compared to 2%Fe-SB-DETA. The result shows that the electron transfer rate of 8%Fe-SB-DETA is stronger than other materials, which is beneficial to pollutants adsorption.

The current density is tested for more than 300 s, maintaining the applied voltage constant at 1.0 mV. Figure 6 shows the currents densities are 0.0045, 0.0050, 0.0084, 0.0063 and 0.0060 mA for 2%Fe-SB-DETA, 4%Fe-SB-DETA, 8%Fe-SB-DETA, 16%Fe-SB-DETA and 32%Fe-SB-DETA, respectively. The current of 8%Fe-SB-DETA is 1.9 times larger than that of 2%Fe-SB-DETA, indicating that doping with iron could significantly enhance electron mobility by reducing the recombination of electron-hole pairs.

Electrochemical impedance spectroscopy is a technique to measure the internal resistance of working electrode material and determine the circuitry and corresponding resistance between the electrolyte and the electrode, like biochar carbon in this case. A sine wave of 1.0 mV amplitude was applied and the frequency was varied from 10 to 10 MHz in the 6 M KOH aqueous solution. Ionic and electronic interactions cause the overall impedance of the materials. The larger value of the Z″ (ohm) is indicative of higher resistance due to the transfer of charges. The overall resistance consists of

Downloaded from http://iwaponline.com/wst/article-pdf/85/5/1384/1021040/wst085051384.pdf
by guest

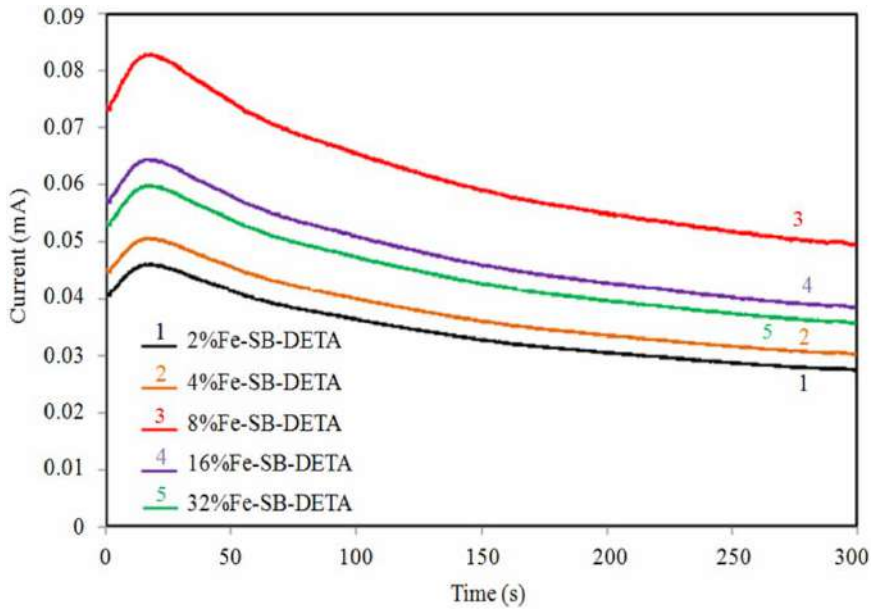

Figure 6 | I-t curves of biochar at the bias potential of 1.0 mV.

electrical resistance, the resistance due to electrolyte, and the resistance for the carbon pore charge transfer as well as the internal resistance of the material. In the results shown in Figure 7, the 2%Fe-SB-DETA produces a high Z″ value, indicative of higher resistance due to the transfer of charges. The smaller Z″ value of 8%Fe-SB-DETA indicates higher charge carrier transfer efficiency. This determines the effective characteristics of materials as adsorption material. 8%Fe-SB-DETA stands out among all five samples as ideal adsorption material with better adsorption capacity.

As(III) adsorption capacity with Fe-SB-DETA

The effect of Fe loading mass onto SB-DETA is also discussed in this study. Fe ratio varies with specific dose applied by $FeCl_3$ during the synthesis process. Different $FeCl_3$ contents, including 2.0, 4.0, 8.0, 16.0 and 32.0%, were evaluated with 1.5 g L^{-1} of 8%Fe-SB-DETA at 0.5 mg L^{-1} As(III) with 30 min contact time. The As(III) adsorption experiment was controlled at pH 3

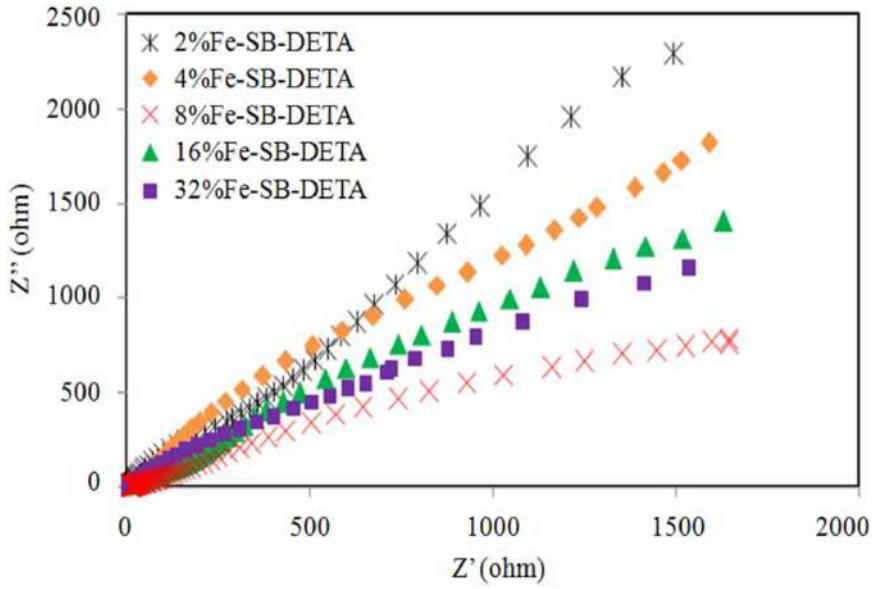

Figure 7 | EIS curve for biochar at the bias potential of 1.0 mV.

Downloaded from http://iwaponline.com/wst/article-pdf/85/5/1384/1021040/wst085051384.pdf
by guest

to obtain optimum operating conditions in this study, because the valence of As(III) was (±) neutral at pH between 2 and 8. However, the valence of As(III) was (–) negative under pH larger than 9. In addition, the surface of 8%Fe-SB-DETA was (+) positively charged at pH between 2 and 3. However, the surface of As(III) was (–) negative under pH larger than 4, as shown in Table 1. Therefore, there is no repulsion between As(III) and 8%Fe-SB-DETA. In this adsorption experiment, first, As(III) is oxidized to form As(V) by 8%Fe-SB-DETA. Afterward, there was electrostatic interaction between As(V) and the material. At the same time, As(V) and the amino functional group on the surface of the material will also produce complexation, so that As(V) is adsorbed on the surface of the material.

The results show that the removal efficiency of arsenic significantly increases from 30 to 90% with increasing Fe content from 2.0 to 16.0%. However, the removal efficiency is not changed obviously from 85 to 90% with increasing Fe content from 8.0 to 16.0%. In contrast, the removal efficiency is decreased from 90 to 66% with increasing Fe content from 16.0 to 32.0%. In this study, it shows that the Fe impregnated on SB-DETA can significantly enhance the adsorption capacity for arsenic. The higher Fe content does not increase removal efficiency too much when Fe is doped on SB-DETA, but causes the pores to be blocked and remain on the surface of the material, resulting in a decrease in pore volume and specific surface area. The higher iron particles covering the surface of the material will directly affect the complexation between the amine functional group and As(V), causing the adsorption effect to decrease. The adsorption capacity of 8% Fe-SB-DETA was calculated as 1.12, 2.23, 3.87, 4.24 and 2.83 mg g^{-1} with Fe content of 2.0, 4.0, 8.0, 16.0 and 32.0%, respectively, as shown in Figure 8. This result is similar to Xiong *et al.* (2017) by iron hydroxide/manganese dioxide doped straw activated carbon.

Mass balance experiment

A mass balance experiment was conducted to understand the mass before and after arsenic adsorption in the adsorption experiment, as shown in Figure 9. The adsorption of As was studied with 20 mg L^{-1} As(III) solution with using 43 g L^{-1} of 8%Fe-SB-DETA material at pH 3 for 30 min contact time. The remaining concentrations and mass of As(III) and As(V) in 0.2 L solution

Table 1 | The effect of material surface charge under different pH conditions

pH	2	3	4	5	6	7	8	9	10	11	pH_{zpc}
As(III)	±	±	±	±	±	±	±	–	–	–	
As(V)	±	–	–	–	–	–	–	–	–	–	
8%Fe-SB-DETA	+	+	–	–	–	–	–	–	–	–	3.87

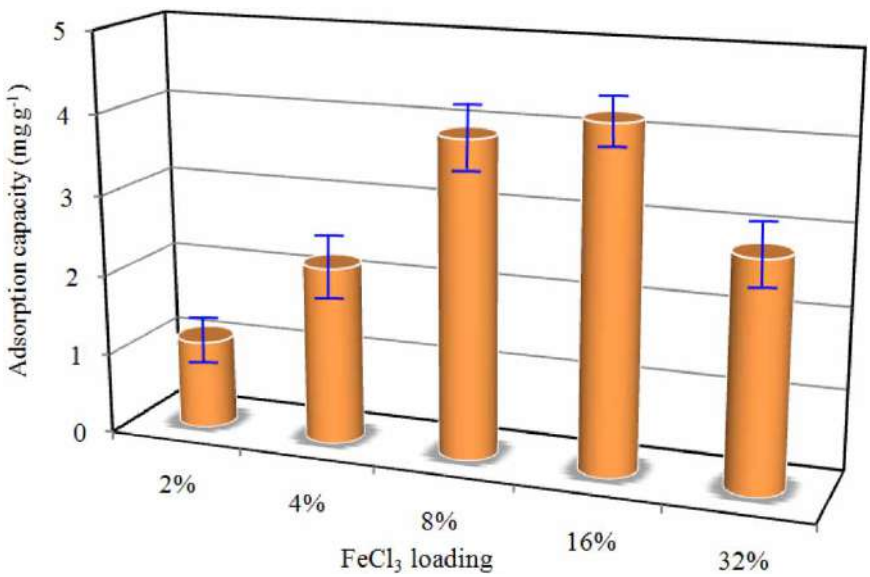

Figure 8 | The effect of Fe loading content on the adsorption efficiency.

Downloaded from http://iwaponline.com/wst/article-pdf/85/5/1384/1021040/wst085051384.pdf
by guest

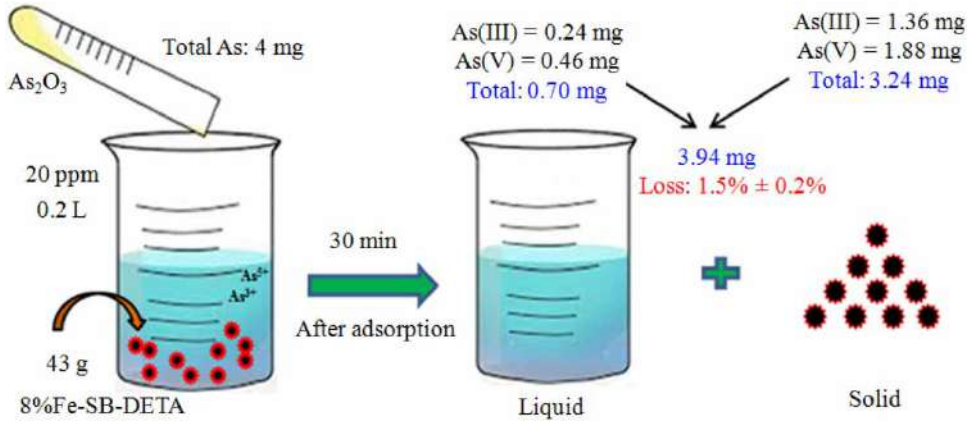

Figure 9 | Schematic diagram of mass balance experiment.

after adsorption are 1.2 ppm and 0.24 mg; 2.3 ppm and 0.46 mg, respectively. In this specific adsorption, As(III) is oxidized to form As(V) by 8%Fe-SB-DETA. This result has been proved by XPS analysis results that Fe^{3+} reduced to Fe^{2+} after As(III) adsorption. Afterward, the iron oxyhydroxides particles located on the SB-DETA surface are capable of replacing the -OH ligand of As(V) molecules, forming mono or bi-dentate complexes allowing them to be attached to the surface. In addition, the 8%Fe-SB-DETA powder was subjected to a dissolution experiment, and the test results showed that the dissolution concentrations and mass of As(III) and As(V) were 6.8 ppm and 1.36 mg; 9.4 ppm and 1.88 mg, respectively. The results show that the total dissolved concentration after arsenic adsorption is 3.94 mg. The concentration of arsenic is 0.06 mg, which is equivalent to 1.5 ± 0.2%. This is caused by the loss of 8%Fe-SB-DETA powder during the dissolution test and filtration process.

Adsorption kinetics

The correlation coefficients (R^2) increased from 0.7026 to 0.7773 when the initial concentration of As(III) increased from 0.2 to 0.8 ppm. However, the values of the rate constant (k_1) were found to increase from 1.8×10^{-3} min^{-1} to 4.4×10^{-3} min^{-1}. The data shows that there is not good compliance with the pseudo first order equation and the regression coefficients for the linear plots were lower than 0.95, which indicates that the pseudo first order equation is not applicable when describing As(III) adsorption behaviors on 8%Fe-SB-DETA materials, as shown in Figure 10(a). In the other hand, the R^2 of pseudo-second-order model range from 0.9733 to 0.9957 with As(III). However, the values of the rate constant (k_2) were found to increase from 2.9×10^{-3} mgg^{-1} min^{-1} to 4.1×10^{-3} mg g^{-1} min^{-1} with As(III). The data shows good compliance with the pseudo second order equation and the regression coefficients for the linear plots were higher than 0.97, which indicates that the pseudo second order equation is applicable when describing As(III) adsorption behaviors on 8%Fe-SB-DETA materials, as shown in Figure 10(b). The finding demonstrates that the adsorption mechanism of As(III) on 8%Fe-SB-DETA includes both physical and chemical adsorption.

Adsorption configurations of arsenic on Fe-SB-DETA

In order to understand the adsorption mechanism of amine functional group and metal functional group complexes for arsenic adsorbed on the surface of SB and Fe-SB-DETA this study used DFT to verify the arsenic adsorption mechanisms by SB and Fe-SB-DETA composite material. In this research, a single layer structure is used to simulate carbon surface models of SB, as shown in Figure 11(a). Figure 11(b) shows that the arsenic was adsorbed onto the SB surface with E_{ads} values of −27.3 kJ mol^{-1}, indicating a physical adsorption between arsenic and the SB surface. This result has proved electrostatic between the positively charged surface of the SB and the anionic arsenic. The results for the adsorption of arsenic on the Fe-SB-DETA surface display all the obtained conformations in Figure 11(c) and 11(d) and Table 2. It also shows that the bond type, bond distance and adsorption energies. Adsorption configurations were considered in Figure 11(c) and 11(d) in order to achieve the most stable arsenic adsorption configuration. The more monodent conformations have been identified, where the interaction of dopant O with the unprotonated O atom belonging to an As-O bond is formed. The bond distances of N-O and Fe-O are 1.84 and 1.42 Å, respectively, are shorter for the compounds in compliance with the increased adsorption energies (−93.5 and −246.3 kJ mol^{-1}), indicating strong chemical adsorption between arsenic and the Fe-SB-DETA surface. In 2016, Wei *et al.* (2016) simulated the adsorption effect of As(V) on TiO_2 at pH 4, results shown the bond distances and E_{ads} of As(V) adsorption configurations on TiO_2 surface

Downloaded from http://iwaponline.com/wst/article-pdf/85/5/1384/1021040/wst085051384.pdf
by guest

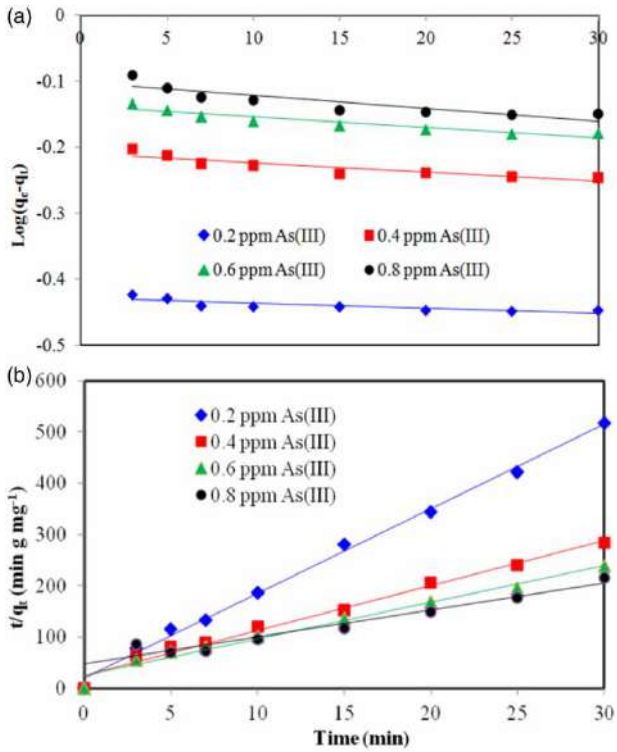

Figure 10 | Adsorption kinetics for adsorption of arsenic: (a) Pseudo-first-order and (b) Pseudo second order.

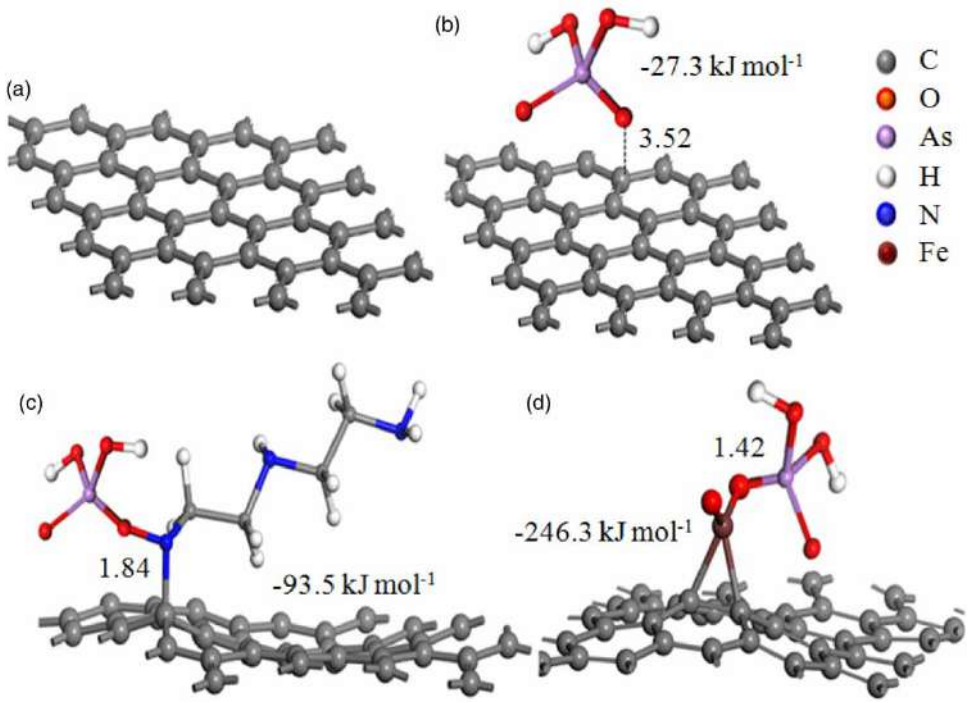

Figure 11 | The adsorption configurations of arsenic on Fe-SB-DETA

were 1.74 Å and 292 KJ mol^{-1}, respectively. The DFT simulation in this study has a limitation, since DFT cannot simulate the adsorption behavior between different iron content and arsenic. If DFT break through this limitation, the DFT simulation results will be more detailed and close to the actual results of this experiment.

Downloaded from http://iwaponline.com/wst/article-pdf/85/5/1384/1021040/wst085051384.pdf
by guest

Table 2 | Adsorption energies of arsenic adsorbed onto Fe-SB-DETA

Pollutant	Bond	Bond distances (Å)	E_{ads} (KJ mol^{-1})
As(III)	C-O (b)	3.52	−27.3
	N-O (c)	1.84	−93.5
	Fe-O (d)	1.42	−246.3

Mechanism discussion of arsenic adsorption on 8%Fe-SB-DETA

The mechanism for the adsorption of arsenic by 8%Fe-SB-DETA material has been proposed with the results obtained from the characteristics analysis, experimental data and kinetic adsorption. The reaction mechanism is divided into four pathways, as presented in Figure 12. In the first pathway, first, As(III) is oxidized to form As (V) by 8%Fe-SB-DETA at pH 3, as shown in the Equation (7). Afterward, the iron oxyhydroxides particles located on the 8%Fe-SB-DETA surface are capable of replacing the -OH ligand of As(V) molecules, forming mono or bi-dentate complexes allowing them to be attached to the surface (Jain *et al.* 1999; Sherman & Randall 2003; Arcibar-Orozco *et al.* 2014), as shown in Equation (8). The second pathway is the interaction of amino functional groups on the surface of 8%Fe-SB-DETA with the As(V) molecule produces a complexation interaction, causing As(V) to be adsorbed on the surface of the material, as shown in Equation (9). In the third pathway, the attachment of As(V) ions onto the 8%Fe-SB-DETA via electrostatic interactions, the surface of the material is positively charged and the As(V) ion is negative charged producing electrostatic adsorption under acidic conditions. In this specific adsorption, the coordination only occurs in charged molecules that were previously attracted to the surface of the 8%Fe-SB-DETA, or in those molecules that have energy enough to counteract the electrostatic repulsion with the 8%Fe-SB-DETA surface. Therefore, in 8%Fe-SB-DETA with a negative surface charge, electrostatic repulsion between the surface and As(V) anions occurs. If these ionic molecules have difficulties in overcoming these electrostatic forces they cannot interact to a higher extent with iron particles and hence adsorption occurs to a lesser extent (Arcibar-Orozco *et al.* 2014). The fourth pathway is the attachment of As(III) and As(V) ions into the pore of 8%Fe-SB-DETA material via physical adsorption, which may be attributed to Van der Waals forces:

$$M - FeOOH + H_3AsO_3 = M - FeO + H_2AsO_4^- + 2H^+ \quad (7)$$

$$M - FeOOH + H_2AsO_4^- + H^+ = M - FeO{-}H_2AsO_4 + H_2O \quad (8)$$

$$M - NH_3 + H_2AsO_4^- = M - NH_2 - H_3AsO_4 \quad (9)$$

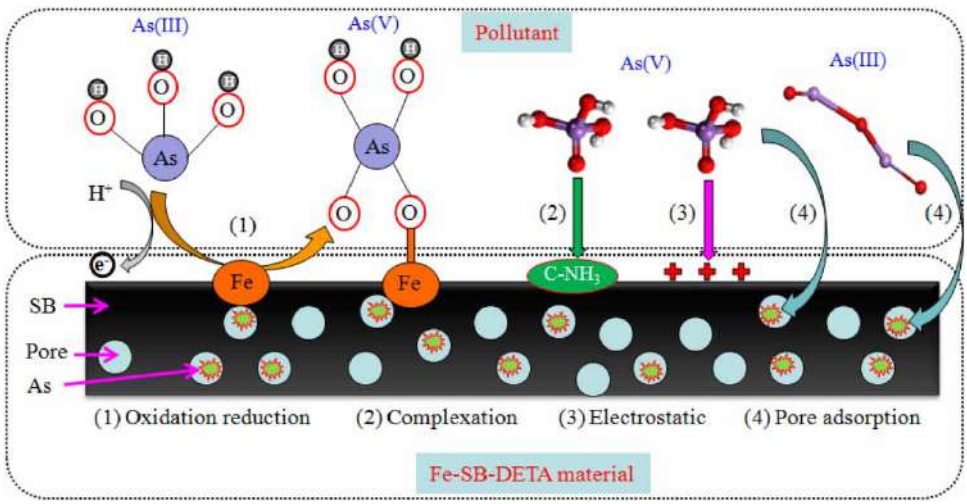

Figure 12 | The mechanism of arsenic adsorption on 8% Fe-SB-DETA.

Downloaded from http://iwaponline.com/wst/article-pdf/85/5/1384/1021040/wst085051384.pdf
by guest

In order to understand whether As(III) is oxidized to As(V), this study uses XPS to detect the material before and after adsorption. The valence state and relative content of As(III) after adsorption was studied with 1.5 g L^{-1} of SB-DETA and 8%Fe-SB-DETA, 0.5 mg L^{-1} As(III) solution, pH 3 and 30 min contact time. XPS peak differentiation-imitating analysis of the As3d spectrum was conducted. The core level spectrum of As3d of the SB-DETA sample reveals the binding energy peaks at 44.3 and 45.5 eV corresponding to As(III) and As(V) core levels, respectively. The percentages of As^{3+} (79.15%) and As^{5+} (20.85%) relative to the total Fe were calculated, mainly As^{3+} valence state, as shown in Figure 13(a). Figure 13(b) shows that the relative content of As^{3+} after adsorption on the surface of 8%Fe-SB-DETA was reduced to 39.65%; meanwhile, that of As^{5+} increased to 60.35%.

To determine the valence state and relative content of Fe in the reaction, XPS peak differentiation-imitating analysis of the Fe2p spectrum was conducted, as shown in Figure 13(c) and 13(d). The core level spectrum of Fe2p of the 8%Fe-SB-DETA sample reveals the binding energy peaks at 714.5 and 728.1 eV corresponding to Fe2p3/2 and Fe2p1/2 core levels, respectively. The photoelectron peaks observed at 714.3 and 717.8 eV corresponded to the binding energies of Fe2p3/2, which suggested that the SB-DETA was covered by a layer of iron oxides/hydroxides of iron, such as FeO, Fe_3O_4 and $Fe(OH)_3$. The percentages of Fe^{3+} and Fe^{2+} relative to the total Fe were calculated. By comparing Figure 13(c) and 13(d), it can be seen that the relative content of Fe^{3+} after the reaction was reduced from 58.28 to 21.88%; meanwhile, that of Fe^{2+} increased from 41.72 to 78.12%. This result is consistent with the mass balance experiment, Fe^{3+} (21.88%) are reduced to Fe^{2+} (78.12%) and As^{3+} (39.65%) are oxidized to As^{5+} (60.35%).

In order to understand whether there is complex adsorption between 8%Fe-SB-DETA and arsenic after modification, the functional group changes of 8%Fe-SB-DETA before and after the adsorption of arsenic under different initial concentrations, 1.5 mg L^{-1} dosage at pH 3 and 30 min, are shown in Figure 14. The intensity of the characteristic peaks at 3400 and 1040 cm^{-1} was significantly reduced when the arsenic concentration increased. This result proved the C-NH_3 function group on the surface of 8%Fe-SB-DETA has generated complexation with the arsenic.

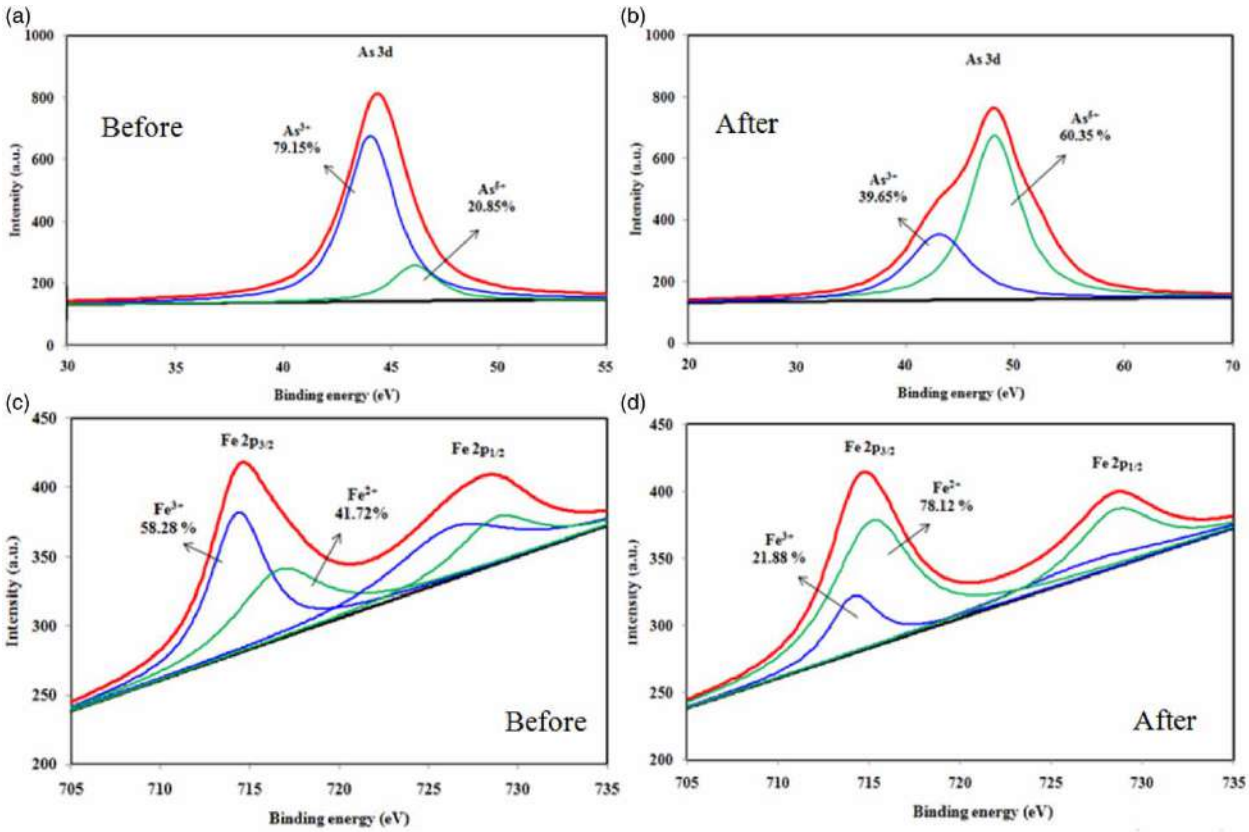

Figure 13 | XPS of the As3d and Fe2p state of arsenic before and after adsorption present in 8%Fe-SB-DETA.

Downloaded from http://iwaponline.com/wst/article-pdf/85/5/1384/1021040/wst085051384.pdf
by guest

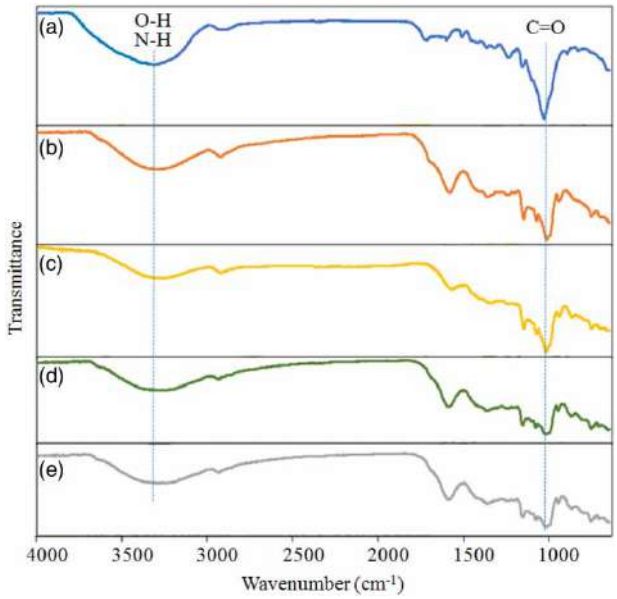

Figure 14 | FTIR spectrums of (a) 8%Fe-SB-DETA and after adsorption As(III) with (b) 0.2 ppm, (c) 0.4 ppm, (d) 0.6 ppm and (e) 0.8 ppm.

CONCLUSIONS

The results clearly demonstrate the feasibility of using urban sludge as a carbon source to produce biochar. Loading amine and iron on sludge biochar greatly improved its As(III) adsorption capacity. ECT result is indicating that 8%Fe-SB-DETA has a larger active point and better oxidation reduction reaction. Therefore, the highest As(III) removal efficiency is 90% and adsorption capacity is 4.24 mg g^{-1}. Simultaneously, the DFT model result is the same as the result of As(III) adsorption performance, because the adsorption energy of Fe-SB-DETA is greater than SB material. The reaction mechanism is divided into four pathways, including oxidation reduction, complexation, electrostatic adsorption and pore adsorption.

DATA AVAILABILITY STATEMENT

All relevant data are included in the paper or its Supplementary Information.

REFERENCES

Aacharya, S., Gaowa, N., Ohashi, H., Kawamoto, D., Honma, T., Okaue, Y. & Yokoyama, T. 2017 Adsorption behavior of arsenic to an isolated ferric ion combined on chelate resin. *Bull. Chem. Soc. Jpn.* **90**, 1372–1374.

Akin, I., Arslan, G., Tor, A., Ersoz, M. & Cengeloglu, Y. 2012 Arsenic (V) removal from underground water by magnetic nanoparticles synthesized from waste red mud. *J. Hazard. Mater.* **235–236**, 62–68.

Aposhian, H. V., Maiorino, R. M., Dart, R. C. & Perry, D. F. 1989 Urinary excretion of meso-2, 3-dimercaptosuccinic acid in human subjects. *Clin. Pharmacol. Ther.* **45**, 520–526.

Arcibar-Orozco, J. A., Josue, D. B., Rios-Hurtado, J. C. & Rangel-Mendez, J. R. 2014 Influence of iron content, surface area and charge distribution in the arsenic removal by activated carbons. *Chem. Eng. J.* **249**, 201–209.

Bhardwaj, A. K., Sundaram, S., Yadav, K. K. & LalSrivastav, A. 2021 An overview of silver nano-particles as promising materials for water disinfection. *Environ. Technol. Innovation* **23**, 101721.

Bhowmick, S., Chakraborty, S., Mondal, P., Van Renterghem, W., Van den Berghe, S., Roman-Ross, G., Chatterjee, D. & Iglesias, M. 2014 Montmorillonite-supported nanoscale zero-valent iron for removal of arsenic from aqueous solution: kinetics and mechanism. *Chem. Eng. J.* **243**, 14–23.

Chen, C. K., Nguyen, N. T., Duong, C. C., Le, T. T., Chen, S. S. & Chang, C. T. 2021 Adsorption configurations of iron complexes on As(III) adsorption over sludge biochar surface. *J. Nanosci. Nanotechnol.* **21**, 5174–5180.

Choong, T. S. Y., Chuah, T. G., Robiah, Y., Koay, F. L. G. & Azni, I. 2007 Arsenic toxicity, health hazards and removal techniques from water: an overview. *Desalination* **217**, 139–166.

Cui, H., Su, Y., Li, Q., Gao, S. & Shang, J. K. 2013 Exceptional arsenic (III, V) removal performance of highly porous, nanostructured ZrO_2 spheres for fixed bed reactors and the full-scale system modeling. *Water Res.* **47**, 6258–6268.

Delley, B. 2002 Hardness conserving semilocal pseudopotentials. *Phys. Rev. B* **66**, 155125.

Downloaded from http://iwaponline.com/wst/article-pdf/85/5/1384/1021040/wst085051384.pdf
by guest

Dong, H., Guan, X. & Lo, I. M. 2012 Fate of As(V) treated nano zero-valent iron: determination of arsenic desorption potential under varying environmental conditions by phosphate extraction. *Water Res.* **46**, 4071–4080.

Feng, Q., Zhang, Z., Ma, Y., He, X., Zhao, Y. & Chai, Z. 2012 Adsorption and desorption characteristics of arsenic onto ceria nanoparticles. *Nanoscale Res. Lett.* **7**, 1–8.

Gao, Z., Li, M., Sun, Y. & Yang, W. 2018 Effects of oxygen functional complexes on arsenic adsorption over carbonaceous surface. *J. Hazard. Mater.* **360**, 436–444.

Hao, L., Zheng, T., Jiang, J., Zhang, G. & Wang, P. 2016 Removal of As(III) and As(V) from water using iron doped amino functionalized sawdust: characterization, adsorptive performance and UF membrane separation. *Chem. Eng. J.* **292**, 163–173.

Hu, L., Peng, Y., Wu, F., Peng, S., Li, J. & Liu, Z. 2017 Tubular activated carbons made from cotton stalk for dynamic adsorption of airborne toluene. *J. Taiwan Inst. Chem. Eng.* **80**, 399–405.

Jain, A., Raven, K. P. & Loeppert, R. H. 1999 Arsenite and arsenate adsorption on ferrihydrite: surface charge reduction and net OH- release stoichiometry. *Environ. Sci. Technol.* **33**, 1179–1184.

Jindo, K., Mizumoto, H., Sawada, Y., Sánchez-Monedero, M. & Sonoki, T. 2014 Physical and chemical characterizations of biochars derived from different agricultural residues. *Biogeosci. Discuss.* **11**, 11727–11746.

Kanwar, V. S., Sharma, A., Srivastav, A. L. & Rani, L. 2020 Phytoremediation of toxic metals present in soil and water environment: a critical review. *Environ. Sci. Pollut. Res.* **27**, 44835–44860.

Karmacharya, M. S., Gupta, V. K., Tyagi, I., Agarwal, S. & Jha, V. K. 2016 Removal of As(III) and As(V) using rubber tire derived activated carbon modified with alumina composite. *J. Mol. Liq.* **216**, 836–844.

Kilic, M., Apaydin-Varol, E. & Pütün, A. E. 2011 Adsorptive removal of phenol from aqueous solutions on activated carbon prepared from tobacco residues: equilibrium, kinetics and thermodynamics. *J. Hazard. Mater.* **189**, 397–403.

Kurniawan, T. A., Sillanpaa, M. E. & Sillanpaa, M. 2012 Nano adsorbents for remediation of aquatic environment: local and practical solutions for global water pollution problems. *Crit. Rev. Env. Sci.Technol.* **42**, 1233–1295.

La, D. D., Nguyen, T. A., Jones, L. A. & Bhosale, S. V. 2017 Graphene supported spinel $CuFe_2O_4$ composites: novel adsorbents for arsenic removal in aqueous media. *Sensors* **17**, 1292.

Lin, M. F., Nguyen, N. T., Chang, C. T. & Chen, P. H. 2019 Preparation of Fe-SBC from urban sludge for organic and inorganic arsenic removal. *J. Nanosci. Nanotechnol.* **19**, 2658–2663.

Ma, Y., Liu, W. J., Zhang, N., Li, Y. S., Jiang, H. & Sheng, G. P. 2014 Polyethylenimine modified biochar adsorbent for hexavalent chromium removal from the aqueous solution. *Bioresour. Technol.* **169**, 403–408.

Mahmood, T., Aslam, M., Naeem, A., Siddique, T. & Din, S. U. 2018 Adsorption of As(III) form aqueous solution onto iron impregnated used tea activated carbon: equilibrium, kinetic and thermodynamic study. *J. Chil. Chem. Soc.* **63**, 3855–3866.

Markandeya, M., Shukla, S. P. & Srivastav, A. L. 2021 Removal of disperse orange and disperse blue dyes present in textile mill effluent using zeolite synthesized from cenospheres. *Water Sci. Technol.* **84**, 445–457.

Materials Studio DMoL^3 2018 *Software Users Manual for Simulate Chemical Processes and Predict Properties of Materials Both Rapidly and Accurately Application*. BIOVIA Company.

Mondal, P., Majumder, C. B. & Mohanty, B. 2006 Laboratory based approaches for arsenic remediation from contaminated water: recent developments. *J. Hazard. Mater.* **137**, 464–479.

Mondal, P., Bhowmick, S., Chatterjee, D., Figoli, A. & Bruggen, B. V. 2013 Remediation of inorganic arsenic in groundwater for safe water supply: a critical assessment of technological solutions. *Chemosphere* **92**, 157–170.

Olyaie, E., Banejad, H., Afkhami, A., Rahmani, A. & Khodaveisi, J. 2012 Development of a cost-effective technique to remove the arsenic contamination from aqueous solutions by calcium peroxide nanoparticles. *Sep. Purif. Technol.* **95**, 10–15.

Perdew, J. P., Burke, K. & Ernzerhof, M. 1996 Generalized gradient approximation made simple. *Phys. Rev. Lett.* **77**, 3865–3868.

Rahman, H. L., Erdem, H., Sahin, M. & Erdem, M. 2020 Iron-incorporated activated carbon synthesis from biomass mixture for enhanced arsenic adsorption. *Water Air Soil Pollut.* **231**, 1–17.

Rani, L., Kaushal, J., Srivastav, A. L. & Mahajan, P. 2020 A critical review on recent developments in MOF adsorbents for the elimination of toxic heavy metals from aqueous solutions. *Environ. Sci. Pollut. Res.* **27**, 44771–44796.

Ray, P. Z. & Shipley, H. J. 2015 Inorganic nano-adsorbents for the removal of heavy metals and arsenic: a review. *RSC Adv.* **5**, 29885–29907.

Reddy, K., McDonald, K. & King, H. 2013 A novel arsenic removal process for water using cupric oxide nanoparticles. *J. Colloid Interface Sci.* **397**, 96–102.

Sahu, M. K. & Patel, R. K. 2013 Adsorption studies of arsenic (III) removal from water by zirconium polyacrylamide hybrid material (ZrPACM-43). *Water Resour. Ind.* **4**, 51–67.

Sherman, D. M. & Randall, S. R. 2003 Surface complexation of arsenic(V) to iron(III) (hydr)oxides: structural mechanism from ab initio molecular geometries and EXAFS spectroscopy. *Geochim. Cosmochim. Acta* **67**, 4223–4230.

Song, P., Yang, Z., Zeng, G., Yang, X., Xu, H., Wang, L., Xu, R., Xiong, W. & Ahmad, K. 2017 Electrocoagulation treatment of arsenic in wastewaters: a comprehensive review. *Chem. Eng. J.* **317**, 707–725.

Srivastav, A. L., Dhyani, R., Ranjan, M., Madhav, S. & Sillanpää, M. 2021 Climate-resilient strategies for sustainable management of water resources and agriculture. *Environ. Sci. Pollut. Res.* **28**, 41576–41595.

Tang, W., Li, Q., Gao, S. & Shang, J. K. 2011a Arsenic(III, V) removal from aqueous solution by ultrafine α-Fe_2O_3 nanoparticles synthesized from solvent thermal method. *J. Hazard. Mater.* **192**, 131–138.

Downloaded from http://iwaponline.com/wst/article-pdf/85/5/1384/1021040/wst085051384.pdf
by guest

Tang, W., Li, Q., Li, C., Gao, S. & Shang, J. K. 2011b Ultrafine α-Fe_2O_3 nanoparticles grown in confinement of in situ self-formed 'cage' and their superior adsorption performance on arsenic (III). *J. Nanopart. Res.* **13**, 2641–2651.

Wei, Z., Liang, K., Wu, Y., Zou, Y., Zuo, J., Arriagada, D. C., Pan, Z. & Hu, G. 2016 The effect of pH on the adsorption of arsenic(III) and arsenic(V) at the TiO_2 anatase [101] surface. *J. Colloid Interface Sci.* **462**, 252–259.

Xiong, Y., Tong, Q., Shan, W., Xing, Z., Wang, Y., Wen, S. & Lou, Z. 2017 Arsenic transformation and adsorption by iron hydroxide/manganese dioxide doped straw activated carbon. *Appl. Surf. Sci.* **416**, 618–627.

Xu, Z., Li, Q., Gao, S. & Shang, J. K. 2010 As(III) removal by hydrous titanium dioxide prepared from one-step hydrolysis of aqueous $TiCl_4$ solution. *Water Res.* **44**, 5713–5721.

Yang, R., Su, Y., Aubrecht, K. B., Wang, X., Ma, H., Grubbs, R. B., Hsiao, B. S. & Chu, B. 2015 Thiol-functionalized chitin nanofibers for As (III) adsorption. *Polymer* **60**, 9–17.

Zhou, Z., Liu, Y., Liu, S., Liu, H., Zeng, G., Tan, X., Yang, C., Ding, Y., Yan, Z. & Cai, X. 2017 Sorption performance and mechanisms of arsenic(V) removal by magnetic gelatin-modified biochar. *Chem. Eng. J.* **314**, 223–231.

First received 6 August 2021; accepted in revised form 26 January 2022. Available online 8 February 2022

Downloaded from http://iwaponline.com/wst/article-pdf/85/5/1384/1021040/wst085051384.pdf
by guest